Emergence of Undulations and Determination of Materials Properties in Large-Scale Molecular Dynamics Simulation of Layered Double Hydroxides

Mary-Ann Thyveetil, Peter V. Coveney,* James L. Suter, and H. Chris Greenwell†

Centre for Computational Science, Department of Chemistry, University College London, 20 Gordon Street, London WC1H 0AJ, United Kingdom

Received April 3, 2007. Revised Manuscript Received July 20, 2007

Layered double hydroxides (LDHs) have generated a large amount of interest in recent years because of their ability to intercalate a multitude of anionic species. Atomistic simulation techniques such as molecular dynamics have provided considerable insight into the behavior of these materials. The advent of supercomputing grids allows us to explore larger-scale models with considerable ease. Here, we present our findings from large-scale molecular dynamics simulations of Mg_2Al-LDHs intercalated with chloride ions. The largest studied system size consists of one million atoms with lateral dimensions of 588 Å × 678 Å. The system exhibits emergent properties, which are suppressed in smaller-scale simulations. Undulatory modes are caused by the collective thermal motion of atoms in the LDH layers. At length scales larger than 20.7 Å, these thermal undulations cause the LDH sheets to interact and the oscillations are damped. The thermal undulations provide information about the materials properties of the system. In this way, we obtain values for the bending modulus of $8.3 \pm 0.4 \times 10^{-19}$ J with in-plane Young's moduli of 63.4 ± 0.5 GPa for a hydrated system and 139 ± 1 GPa for the LDH sheets alone.

1. Introduction

Layered double hydroxides (LDHs), also known as anionic clays, play a diverse role in many chemical interactions, leading to growing interest in their structure and particularly the organization of the intercalated species within the LDH sheets. Current applications of LDHs cover a wide variety of areas including catalysis,[1] absorbents of anionic species,[2,3] photochemistry,[1,4] and additives in functional polymers,[5,6] electrochemistry,[7,8] and pharmaceuticals.[9,10]

The structure of LDHs is based on that of brucite, which has the formula $Mg(OH)_2$. Unlike brucite, LDH sheets are positively charged, as divalent cations are partially replaced with trivalent cations, resulting in a net charge. Hydroxide groups are arranged around cations octahedrally, as shown in Figure 1. LDHs follow the structural formula $[M^{II}_{1-x}M^{III}_x(OH)_2]^{x+}(A^{n-})_{x/n}\cdot yH_2O$, where M^{II} are divalent cations such as Mg, Mn, Fe, Co, Ni, Cu, and Zn, M^{III} are trivalent cations such as Al, Mn, Fe, Co, Ni, Cr, Ga, and A^{n-} are interlayer anions that consist of a wide variety of inorganic and organic species. In the present paper, we investigate $[Mg_2Al(OH)_6]Cl\cdot 2H_2O$, which has a similar structure to hydrotalcite, except that the interlayer carbonate ions are replaced by chloride ions.

There has recently been a large amount of work dedicated to the simulation of smectite clays, also called cationic clays. Although classified separately, smectites are similar to LDHs in that part of their structure contains cations octahedrally coordinated with oxygen atoms.[11] Both materials also form thin platelets that are between 100−1000 nm in diameter. These structural similarities mean that similar experimental and simulation techniques can be used to analyze both types of clay materials.[11] Molecular dynamics techniques have been widely employed to understand important structural features in smectites and LDHs, such as the behavior of the interlayer region,[11−19] which are difficult to obtain experimentally.

* To whom correspondence should be addressed. E-mail: p.v.coveney@ucl.ac.uk.

† Present address: Department of Chemistry, University of Durham, South Road, Durham DH1 3LE, U.K.

(1) Takagi, K.; Shichi, T.; Usami, H.; Sawaki, Y. *J. Am. Chem. Soc.* **1993**, *115*, 4339−4344.
(2) Das, D. P.; Das, J.; Parida, K. *J. Colloid Interface Sci.* **2003**, *261*, 213−220.
(3) Perez, M. R.; Pavlovic, I.; Barriga, C.; Cornejo, J.; Hermosin, M. C.; Ulibarri, M. A. *Appl. Clay Sci.* **2006**, *32*, 245−251.
(4) Shichi, T.; Minamikawa, Y.; Yasuda, N.; Yamada, N.; Okamoto, Y.; Takagi, K. *Chem. Lett.* **2003**, *32*, 240−241.
(5) van der Ven, L.; van Gemert, M. L. M.; Batenburg, L. F.; Keern, J. J.; Gielgens, L. H.; Koster, T. P. M.; Fischer, H. R. *Appl. Clay Sci.* **2000**, *17*, 25−34.
(6) Wang, X. D.; Zhang, Q. *Polym. Int.* **2004**, *53*, 698−707.
(7) Chen, H.; Wang, J. M.; Pan, T.; Zhao, Y. L.; Zhang, J. Q.; Cao, C. N. *J. Electrochem. Soc.* **2003**, *150*, 1399−1404.
(8) Ballarin, B.; Morigi, M.; Scavetta, E.; Seeber, R.; Tonelli, D. *J. Electrochem. Soc.* **2000**, *492*, 7−14.
(9) Aisawa, S.; Ohnuma, Y.; Hirose, K.; Takahashi, S.; Hirahara, H.; Narita, E. *Appl. Clay Sci.* **2005**, *28*, 137−145.
(10) Ambrogi, V.; Fardella, G.; Grandolini, G.; Perioli, L. *Int. J. Pharm.* **2001**, *220*, 23−32.
(11) Greenwell, H. C.; Jones, W.; Coveney, P. V.; Stackhouse, S. *J. Mater. Chem.* **2006**, *16*, 708−723.
(12) Greenwell, H. G.; Bowden, A. A.; Chen, B.; Boulet, P.; Evans, J. R. G.; Coveney, P. V.; Whiting, A. *J. Mater. Chem.* **2006**, *16*, 1082−1094.
(13) Greenwell, H. G.; Harvey, M. J.; Boulet, P.; Bowden, A. A.; Coveney P. V.; Whiting, A. *Macromolecules* **2005**, *38*, 6189−6200.
(14) Greenwell, H. G.; Jones, W.; Newman, S. P.; Coveney, P. V. *J. Mol. Struct.* **2003**, *647*, 75−83.
(15) Newman, S. P.; Di Cristina, T.; Coveney, P. V.; Jones, W. *Langmuir* **2002**, *18*, 2933−2939.
(16) Newman, S. P.; Williams, S. J.; Coveney, P. V.; Jones, W. *J. Phys. Chem. B* **1998**, *102*, 6710−6719.

10.1021/cm070923u CCC: $37.00
Published on Web 10/10/2007

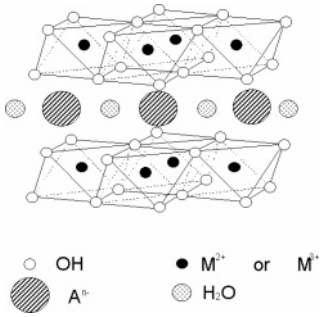

Figure 1. Basic structure of layered double hydroxides, formed from positively charged sheets of cations octahedrally coordinated with hydroxide groups. Counterions and water molecules reside within the interlayer region. In the present paper, we study the case where M^{2+} and M^{3+} are Mg^{2+} and Al^{3+} ions, respectively, and the interlayer A^{n-} ion is Cl^-.

Periodic boundary conditions are usually invoked in atomistic simulations to simulate bulk behavior without modeling extremely large numbers of atoms. Although this method has many advantages, it can lead to unrealistic behavior in some situations. The purpose of the present paper is to investigate such finite-size effects and their elimination through the study of the properties of increasingly large models. The same approach was adopted in a previous study by us where emergent undulations of smectite clay sheets were observed.[20] These undulations can be used to calculate materials properties such as the bending and Young's moduli.[20]

Finite-size effects arise in simulations when the properties being studied depend on the number of atoms in the simulation cell. Short-range interactions are usually not affected by periodic boundaries, but it is often difficult to avoid finite-size effects with long-range interactions such as electrostatic forces. The LDH systems we are modeling turn out to exhibit very significant finite-size effects, one manifestation of which is the emergence of collective thermal undulations of the atoms within the clay sheets, which are suppressed by the periodic boundaries in smaller models. This effect has previously been observed by Suter et al. in smectite clays.[20,12]

The advent of high-performance grid computing facilitates simulations performed over longer time and length scales that now approach life-size particles. In large-scale simulations of montmorillonite clay sheets with lateral dimensions greater than 150 Å, thermal fluctuations are observed that can be used to calculate elastic properties of the material.[20] Estimates of the bending, compressibility, and Young's moduli were thereby obtained. Anionic clays are known to be less rigid than cationic clays.[21] As an illustration of this, scanning electron microscopy (SEM) images of LDH−adipate $[Mg_2Al(OH)_6]\cdot 0.5[O_2C(CH_2)_4CO_2]\cdot xH_2O$ are shown in Figure 2, for which the exact water content is undetermined. The SEM images demonstrate the flexibility of LDH sheets as they show that the material can form crumpled structures. This suggests that thermal fluctuations should be evident at smaller length scales in simulations of layered double hydroxides. In the present article, the methodology we used to calculate materials properties for smectite clays[20] is applied to the LDH $[Mg_2Al(OH_6)]Cl\cdot 2H_2O$. Here, we report our findings from large-scale molecular dynamics simulations, extending up to system sizes of one million atoms.

The paper is organized as follows. In Section 2, we describe the methods needed to perform our large LDH simulations. The form of the molecular mechanics forcefield is first outlined, followed by the model construction and its energy minimization. Grid-computing techniques are invaluable in performing such large-scale molecular dynamics simulations. The supercomputing resources are outlined, as well as the software and visualization tools used. Because this paper uses the techniques developed by Suter et al.,[20] we only outline these here. In Section 3, we report the results we have obtained. The section begins by reporting "local" properties that might be expected to be independent of simulation cell size. This is followed by results for the bending modulus obtained from spectral analysis of the undulatory modes and Young's moduli for the stress−strain deformations. In the final section, we present our conclusions and discuss possible extensions to our work.

2. Methods

2.1. Potential Parametrization. The forcefield used to model our systems is ClayFF, parametrized by Cygan et al.[22] The forcefield treats cations within the clay layer as nonbonded ionic species.[22] The parametrization of ClayFF uses a set of simple, well-characterized hydrated phases that allow a high degree of transferability. When it is applied to smectite clays, close agreement is found with experiment.[23,19] ClayFF also produces good agreement with experiment for layered double hydroxides in terms of lattice parameters, water diffusion coefficients, and far-infrared spectra.[24−27] ClayFF is a class I forcefield: it consists only of bonded, angle, van der Waals, and electrostatic forces. It has the functional form

$$V = V_b + V_{nb} \quad (1)$$

where V is the potential energy of the system, made up of the bonded V_b and nonbonded V_{nb} interaction energies. The

(17) Aicken, A. M.; Bell, I. S.; Coveney, P. V.; Jones, W. *Adv. Mater.* **1997**, *9*, 496−500.
(18) Boulet, P.; Coveney, P. V.; Stackhouse, S. *Chem. Phys Lett.* **2004**, *389*, 261−267.
(19) Greathouse, J. A.; Cygan, R. T. *Phys. Chem. Chem. Phys.* **2005**, *7*, 3580−3586.
(20) Suter, J. L.; Coveney, P. V.; Greenwell, H. C.; Thyveetil, M.-A. *J. Phys. Chem. C.* **2007** *111*, 8248−8259.
(21) Solin, S. A.; Hines, D.; Yun, S. K.; Pinnavaia, T. J.; Thorpe, M. F. *J. Non-Cryst. Solids* **1995**, *182*, 212−220.
(22) Cygan, R. T.; Liang, J.-J.; Kalinichev, A. G. *J. Phys. Chem. B* **2004**, *108*, 1255−1266.
(23) Skipper, N. T.; Lock, P. A.; Titiloye, J. O.; Swenson, J.; Mirza, Z. A.; Howells, W. S.; Fernandez-Alonso, F. *Chem. Geol.* **2006**, *230*, 182−196.
(24) Wang, J.; Kalinichev, A. G.; Kirkpatrick, R. J.; Hou, X. *Chem. Mater.* **2001**, *13*, 145−150.
(25) Kalinichev, A. G.; Kirkpatrick, R. J. *Chem. Mater.* **2002**, *14*, 3539−3549.
(26) Wang, J.; Kalinichev, A. G.; Amonette, J. E.; Kirkpatrick, R. J. *Am. Mineral.* **2003**, *88*, 398−409.
(27) Wang, J.; Kalinichev, A. G.; Kirkpatrick, R. J. *Geochim. Cosmochim. Acta* **2006**, *70*, 562−582.

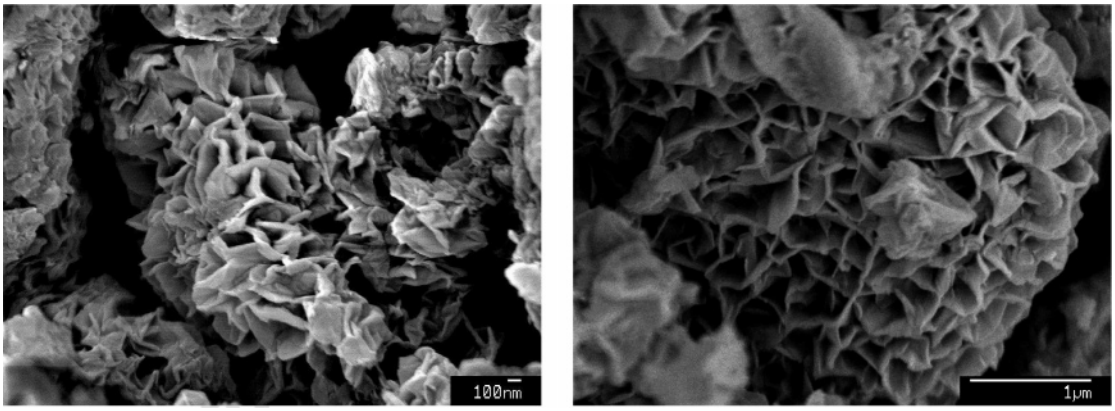

Figure 2. Scanning electron microscopy images of LDH−adipate agglomerates, with chemical formula $[Mg_2Al(OH)_6]\cdot 0.5[O_2C(CH_2)_4CO_2]\cdot xH_2O$. The images show that LDHs are flexible enough to form crumpled structures.

bonded energy of the system can be further broken down into

$$V_b = V_{bs} + V_{ab} \tag{2}$$

where V_{bs} is the bond-stretching term, described as

$$V_{bs} = \sum_{i \neq j} k_1 (r_{ij} - r_0)^2 \tag{3}$$

while V_{ab} describes the angle-bending energies

$$V_{ab} = \sum_{i \neq j \neq k} k_2 (\theta_{ijk} - \theta_0)^2 \tag{4}$$

The parameters k_1, k_2, r_0, and θ_0 are specified within the ClayFF forcefield: r_{ij} represents the distance between pairs of atoms i and j while θ_{ijk} represents the angle formed between three atoms i, j, and k. The nonbonded interaction energy is decomposed into van der Waals and Coulombic terms. The van der Waals potential has the form

$$V_{vdW} = \sum_{i \neq j} D_{o,ij} \left[\left(\frac{R_{o,ij}}{r_{ij}} \right)^{12} - 2 \left(\frac{R_{o,ij}}{r_{ij}} \right)^{6} \right] \tag{5}$$

where $D_{o,ij}$ and $R_{o,ij}$ are the collision diameter and well depth of the Lennard-Jones potential, respectively. The Coulombic potential[28] is written

$$V_{coul} = \frac{e^2}{4\pi\epsilon_0} \sum_{i \neq j} \frac{q_i q_j}{r_{ij}} \tag{6}$$

where q_i and q_j are the charges of atoms i and j, respectively. All parameters are derived from fitting properties of the model to observed structural and physical property data.

The ClayFF partial charges can be found in the paper by Cygan et al.[22] Although most of the original parameters we used were taken from ClayFF, the partial charges were adjusted to maintain electroneutrality for LDHs, as done for previous simulations of layered double hydroxides by Wang et al.,[27,24] who changed the partial charge on oxygen in hydroxyl groups from −0.9500 to −0.9742. With this modification of the ClayFF forcefield, several previous molecular dynamics simulations have been carried out, yielding results in good agreement with experimental observations.[24,26,27] Water molecules were modeled using the flexible single-point charge (SPC) model.[29]

Table 1. Simulation Cell Composition and Dimensions for the Simulated LDH−Water Systems

system	no. of atoms	unit cell replication	no. of water	no. of Cl^-	starting supercell dimensions (Å^3)
I	7 128	3 × 3 × 1	648	324	49.0 × 56.5 × 25.3
II	50 688	8 × 8 × 1	4 608	2 304	130.7 × 150.6 × 25.3
III	256 608	18 × 18 × 1	23 328	11 664	294.2 × 338.8 × 25.3
IV	1 026 432	36 × 36 × 1	93 312	46 656	588.3 × 677.7 × 25.3

2.2. Model Construction. To explore finite-size effects imposed by periodic boundary conditions, our simulations consisted of four different sized models of $[Mg_2Al(OH)_6]$-$Cl\cdot 2H_2O$. The dimensions and compositions of the models are detailed in Table 1. The primitive LDH structure was obtained by the refinement of powder X-ray diffraction data on hydrotalcite using Rietveld methods.[30] The literature reports that two main polytypes of LDH exist: one consisting of a two-layer hexagonal stacking sequence, called 2H, and one consisting of a three-layer rhombohedral unit cell, 3R. Hexagonal stacking of the brucite-like layers is characterized by the $P\bar{6}_3/mmc$ space group, whereas rhombohedral stacking is described by the $R\bar{3}m$ space group.[31] The $R\bar{3}m$ space group is the structure we used, as this is the most commonly found in nature.[32] In addition, hydroxide groups in consecutive layers can be stacked in many different ways, which results in even more possible polytype structures. Bookin and Drits systematically derived all the possible polytypes of LDHs.[33] These authors determined that there were nine different polytypes with a three-layer rhombohedral structure. The stacking of hydroxide groups was a structural feature undetermined in the crystallographic cell used to model our systems, although we later analyzed the stacking of cations in consecutive layers to ascertain whether our models have arranged themselves into a particular polytype.

(28) Hockney, R. W.; Eastwood, J. W. *Computer Simulation Using Particles*; New York: McGraw-Hill, 1981.

(29) Berendsen, H. J. C.; Postma, J. P. M.; van Gunsteren, W. F.; Hermans, J. *Intermolecular Forces*, first ed.; Reidel Publishing Co.: Dordrecht, The Netherlands, 1981.

(30) Bellotto, M.; Rebours, B.; Clause, O.; Lynch, J.; Bazin, D.; Elkaim, E. *J. Phys. Chem.* **1996**, *100*, 8527−8534.

(31) Drits, V. A.; Bookin, A. S. *Appl. Clay Sci.* **2002**, *22*, 75−76.

(32) de la Calle, C.; Pons, C.-H.; Roux, J.; Rives, V. *Clays. Clay. Miner.* **2003**, *51*, 121−132.

(33) Bookin, A. S.; Drits, V. A. *Clays. Clay. Miner.* **1993**, *41*, 551−557.

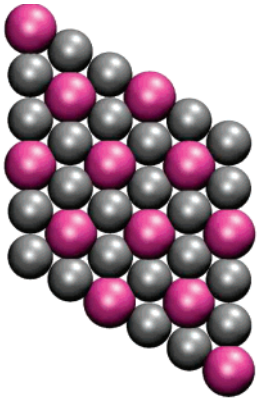

Figure 3. Primitive structure of hydrotalcite-like material simulated in this study. Cationic ordering in the hydrotalcite-like model with Mg^{2+} ions is represented in gray and Al^{3+} is represented in pink. The structure is arranged such that no two aluminum ions are adjacent to one another.

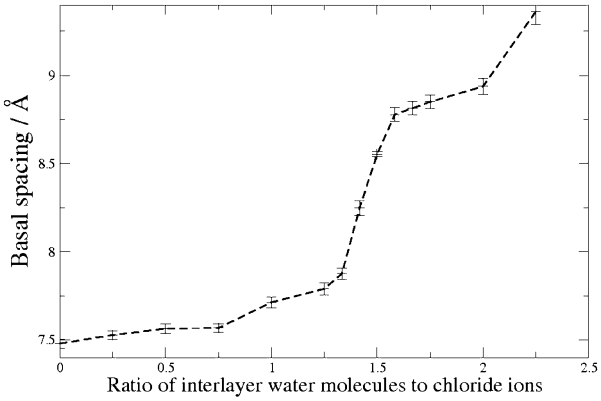

Figure 4. Hydration curve for $[Mg_2Al(OH)_6]Cl{\cdot}nH_2O$. The basal spacing exhibits a rapid increase between H_2O/Cl ratios of 1.25 and 2. Error bars calculated from the standard deviation of the cell parameters.

Our large-scale models were created by replication of a primitive crystallographic cell; this imposes an artificial periodicity, implying cationic ordering in the LDH sheets. However, cationic ordering is likely to exist in nature, as it has been shown by electronic structure simulations that maximizing the distance between Al^{3+} ions is energetically favorable.[34,35] Therefore, the models used in the simulations had aluminum ions placed such that no Al^{3+} ions were adjacent to one another, as shown in Figure 3.

The exact ratio of water molecules to anions in the interlayer region has not been precisely determined experimentally. The disordered nature of the intragallery region makes it difficult to determine this ratio. The value of two H_2O molecules per Cl^- ion has been estimated from thermogravimetric analysis (TGA).[30,36] We carried out preliminary small-scale simulations of the LDH system at different hydration states to explore the change in basal spacing. Figure 4 shows that the hydration curve of our LDH system has a large step between water/Cl^- ratios of 1.25 and 2. A similar pattern of behavior is seen in smectites.[37,38] Unlike smectite clays, however, there does not exist a wealth of experimental data for the swelling of LDHs. Experimental results for $[Mg_2Al(OH)_6]Cl{\cdot}nH_2O$ show that, at room temperature, this material has a basal spacing of 7.8 Å.[36] Although this differs from the simulated value of 8.9 Å, it can be argued that the simulation is a simplified system consisting of a constant number of water molecules, whereas experimentally the water content is much more variable. The large step in Figure 4 also highlights the possibility that the LDH structure may exist with a range of basal spacings at room temperature, an observation that is consistent with the breadth of many LDH X-ray powder diffraction patterns. Therefore, the most accurate way to compare experimental and simulated basal spacings is at a water/Cl^- ratio of 0. In an anhydrous state, experimental measurements yield a basal spacing of 7.5 Å,[36] while our simulations produce a basal spacing of 7.48 ± 0.03 Å, in excellent agreement. Our larger simulation models were built with two H_2O molecules per Cl^- ion in order to be consistent with TGA results.

The crystallographic unit cell was replicated to create a small $6 \times 6 \times 1$ supercell. This structure was provided by Kalinichev and co-workers, who used it previously to carry out several simulations that reproduced experimental properties such as basal spacing and lattice parameters.[24,26,27] Further replication of the model produced the model system sizes detailed in Table 1.

2.3. Energy-Minimization Procedure. Before replicating the system to produce larger models, an initial energy-minimized system was used as a starting structure. The model was minimized using the steepest-descent algorithm[39] followed by the conjugative-gradient algorithm.[40] Because the initial structure was taken from Rietveld analysis and X-ray diffraction data, the interlayer arrangement was not known. This meant careful minimization was required to obtain a structure before simulating it with molecular dynamics. To prevent the system getting trapped in a local potential minimum, the clay layers were initially kept fixed in place, while the interlayer was energy minimized. The constraints on the clay layers were then relaxed, and the potential energy of the whole system was minimized. The simulation cell remained rectilinear in shape, but the cell dimensions were allowed to vary in each dimension.

2.4. Molecular Dynamics Techniques. The large-scale atomistic/molecular massively parallel simulator (LAMMPS)[41] was used to simulate the LDH systems because of its highly scalable nature. The models studied were all simulated for 1.50 ns using the Verlet algorithm and a time step of 0.5 fs. The system was first allowed to equilibrate for 500 ps, and careful monitoring of the potential energy was carried out to make sure the system had reached equilibrium. The final production run was performed over 1 ns. The simulations were carried out using an NPT ensemble throughout together with a Nosé−Hoover thermostat/barostat to regulate the temperature and pressure. The pressure in

(34) Trave, A.; Selloni, A.; Goursot, A.; Tichit, D.; Weber, J. *J. Phys. Chem. B* **2002**, *106*, 12291−12296.
(35) Giese, R. F. *Clays. Clay Min.* **1975**, *23*, 165−166.
(36) Vera, R. L.; Pinnavaia, T. J. *Inorg. Chem.* **1995**, *34*, 883−892.
(37) Cases, J. M.; Berend, I.; Besson, G.; Francois, M.; Uriot, J. P.; Thomas, F.; Poirier, J. E. *Langmuir* **1992**, *8*, 2730−2739.
(38) Hensen, E. J. M.; Smit, B. *J. Phys. Chem. B* **2002**, *106*, 12664−12667.
(39) Arfken, G. *Mathematical Methods for Physicists*, third ed.; Academic Press: New York, 1985.
(40) Hestenes, M. R.; Stiefel, E. *J. Res. Nat. Bur. Stand. (U. S.)* **1952**, *49*, 409−436.
(41) Plimpton, S. *J. Comput. Phys.* **1995**, *117*, 1−19.

Table 2. Average Potential Energy and Cell Dimensions Obtained after 1.5 ns of Simulation; Error Bars Obtained from the Standard Deviation of the Data

system	potential energy normalized with respect to system size (eV)	average x (L_x) (Å)	average y (L_y) (Å)	average z (L_z) (Å)
I	-53.55 ± 0.01	48.1 ± 0.05	55.6 ± 0.05	26.9 ± 0.05
II	-53.556 ± 0.004	128.8 ± 0.05	148.7 ± 0.06	26.8 ± 0.02
III	-53.565 ± 0.002	288.7 ± 0.05	333.3 ± 0.05	26.83 ± 0.009
IV	-53.550 ± 0.001	579.2 ± 0.05	668.7 ± 0.06	26.94 ± 0.005

each dimension was allowed to dilate and contract independently. The simulations were performed at a temperature of 300 K and the pressure was kept at 1 atm, with a damping parameter of 0.5 ps to regulate the pressure control. Electrostatics were computed using the particle−particle particle−mesh (PPPM) algorithm[28] with a precision value of 0.001 and a grid order of 4. The real-space component of the electrostatic forces and the Lennard-Jones potential were assigned cutoffs of 9 and 10 Å, respectively. The extra skin distance for building neighbor lists was set to 2 Å. Snapshots of the positions and velocities of the atoms were taken every 2 ps. At the time of study, LAMMPS only allowed rectilinear cell sizes, which limited the exploration of stacking order in our models.

The atomic density profiles reveal the distribution of certain atom types over the length of the simulation. This is a good measure of any patterns in behavior, particularly when looking at the interlayer region. The one-dimensional atomic density profile orthogonal to the LDH sheet is found by dividing the simulation cell into a two-dimensional grid in either the *xy* or *xz* dimensions, and the number of atoms of a particular element was counted within the projected volume. The *z* direction is orthogonal to the LDH layers. The grid elements were ∼0.1 Å in length. The average atomic density is taken from snapshots throughout the production phase of the simulation. This method assumes that there is negligible variation in cell dimensions, as confirmed by the small standard deviations during the production phase of the simulation, shown in Table 2. The atomic density profile was also expanded to find the average distribution of certain atoms within the *xy* plane, which runs parallel to the LDH sheets, as previously employed when examining the average distribution of interlayer atoms in clays.[42,43]

Molecular dynamics simulations also provide diffusion coefficients that can be compared with experimental data. The movement of water within clay sheets is extremely restricted; water may diffuse in the *xy* dimensions but not in the third *z* dimension. In the LDH systems under study here, the self-diffusion coefficient, *D*, of intercalated water can be found using the formula

$$D = \frac{1}{4}\frac{\mathrm{d}}{\mathrm{d}t}\langle|\mathrm{r}(t) - \mathrm{r}(0)|^2\rangle \qquad (7)$$

where $\langle|\mathrm{r}(t) - \mathrm{r}(0)|^2\rangle$ is the mean square displacement (MSD) of a diffusing atom in two dimensions and *t* is the time. A plot of MSD vs time should exhibit a linear region with a slope of 4*D*.

2.5. Grid-Computing Resources. The computational demand of these simulations meant that very substantial resources were needed to perform the simulations in a reasonable length of real time. Grid-computing facilities in Europe and the U.S. have been utilized to carry out these studies. The simulations were performed using the following federated grid infrastructures: the U.K.'s National Grid Service (www.ngs.ac.uk), including HPCx (www.hpcx-.ac.uk); the U.S. TeraGrid (www.teragrid.org); and the EU Distributed European Infrastructure for Supercomputing Applications (www.deisa.org). System **IV** was the largest model for which simulations were carried out, consisting of 1 026 432 atoms and requiring 50 000 CPU h to complete. Submission of jobs was facilitated by the Application Hosting Environment (AHE) (http://www.omii.ac.uk/).[44] The AHE allows the submission of geographically distributed jobs through a single uniform interface that interoperates between Globus and Unicore grids and also retrieves output data automatically once a simulation has finished.

2.6. Visualization. Visualization provides crucial qualitative insight into the emergent properties of large-scale materials systems[20] and has led us to develop more quantitative analysis techniques. Visualizing large models such as those in our study is a challenge in itself as we are interested in the collective, as well as atomistic, behavior of the system. Efficient algorithms are needed to suitably represent large numbers of atoms. We use the parallel visualization software AtomEye because it renders large numbers of atoms with reasonable efficiency.[45] AtomEye is freely available for Unix systems and renders a scene efficiently by treating atoms and bonds as primitive spheres and cylinders. Additionally, *z*-buffering and volume-clipping algorithms accelerate the rendering process. AtomEye is particularly beneficial for minerals and polymer systems, as it correctly represents periodic boundary conditions. We made use of UCL's SGI Prism, a dedicated visualization facility that allows AtomEye to run on up to six processors and substantially accelerates the rendering process (by 75% for models as large as 1 million atoms).

Our large models greatly benefited from visualization, because it is then immediately apparent that the LDH sheets are very far from rigid. Thermal undulations emerge in larger systems that are suppressed in smaller models. Figure 5 demonstrates this phenomenon more clearly; see also the Supporting Information for a set of animations of the undulations. These effects are discussed in more detail below.

2.7. Spectral Analysis of Thermal Undulations. On large length scales, when the thickness of the LDH sheets is much smaller than the lateral dimensions, each clay sheet can be treated as a continuous surface. Analysis of undulations can then be studied with the Landau−Helfrich

(42) Wang, J.; Kalinichev, A. G.; Kirkpatrick, R. J. *Geochim. Cosmochim. Acta* **2006**, *70*, 562−582.
(43) Hou, X.; Kalinichev, A. G.; Kirkpatrick, R. J. *Chem. Mater.* **2002**, *14*, 2078−2085.
(44) Coveney, P. V.; Saksena, R. S.; Zasada, S. J.; McKeown, M.; Pickles, S. *Comput. Phys. Commun.* **2007**, *176*, 406−418.
(45) Li, J. *Modell. Simul. Mater. Sci. Eng.* **2003**, *11*, 173−177.

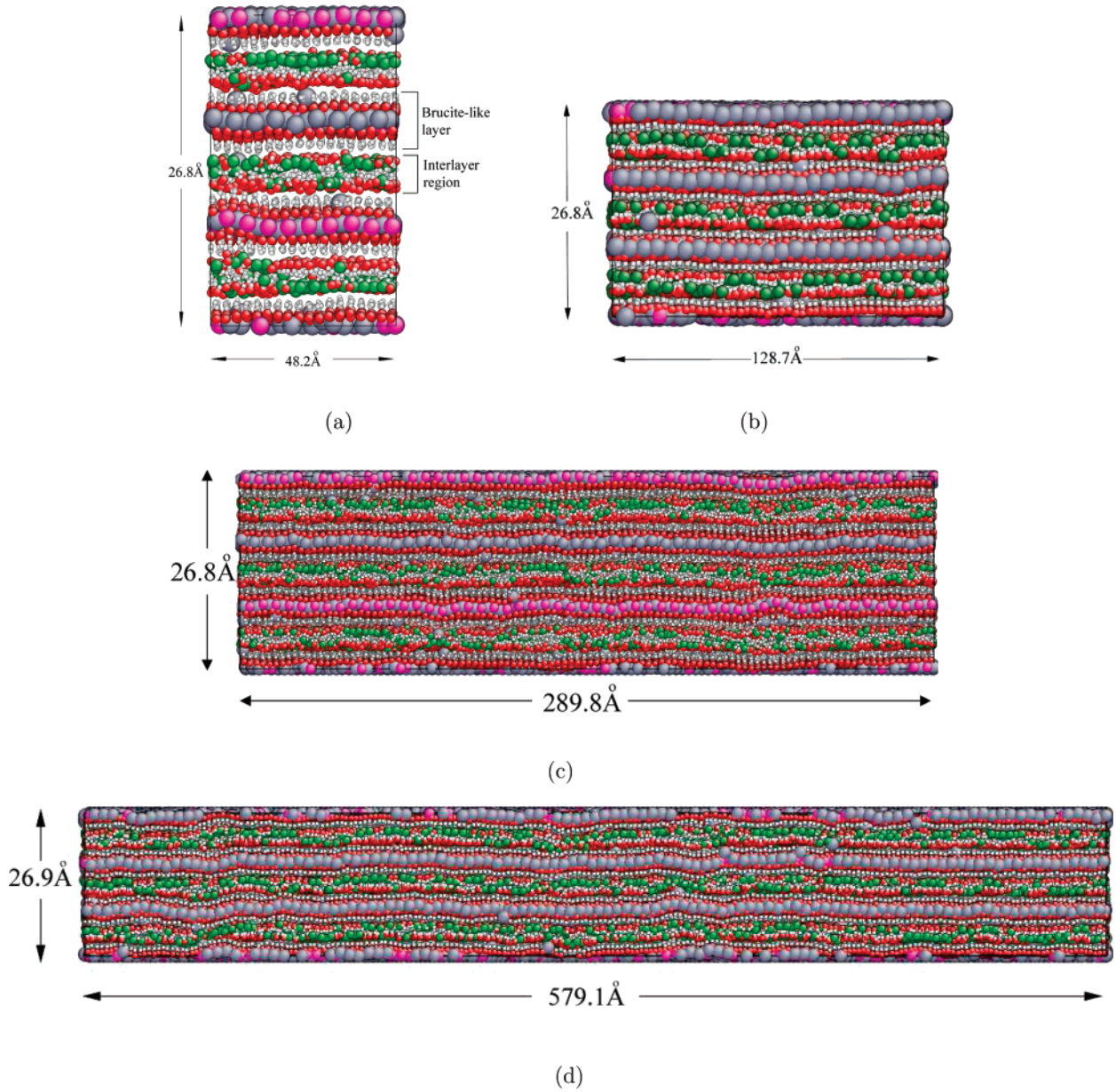

Figure 5. Visualization of (a) system **I**, (b) system **II**, (c) system **III**, and (d) system **IV**. The visualizations have been expanded three times in the *z* direction to aid viewing. The visualizations in the *xy* plane clearly show the development of thermal undulations with supercell size. (a) Shows that the cationic layer is comparatively straighter than that in (d), where waves caused by thermal fluctuations can be seen; see Supporting Information for animations of these undulations. Visualization (a) also shows that a double layer of chloride ions and water molecules has formed, with water oxygen atoms and chloride ions closest to the surface of the clay forming loose hydrogen bonds with hydroxide groups. Magnesium, aluminum, chloride, oxygen, and hydrogen are represented as gray, pink, green, red, and white spheres, respectively.

free energy relating the elastic energy to the shape of the sheet:[46]

$$F = \int_S \mathrm{d}A\left[\gamma + \frac{k_c}{2}(c_1 + c_2 + 2c_0)^2 + k_G c_1 c_2\right] \qquad (8)$$

The integral is performed over the whole surface, S, with respect to the area A; γ represents the surface tension, k_c represents the bending modulus, and k_G represents the saddle-splay/Gaussian curvature modulus.[47,48] The parameters c_1 and c_2 are the principal curvatures of the surface, and c_0 is the spontaneous curvature that is set to 0 when the system is embedded in an isotropic environment.

The Landau−Helfrich free energy can be manipulated in order to find the bending modulus of the clay system. If a two-dimensional discrete Fourier transform is carried out on the LDH sheets, the thermal undulations can be decomposed into a continuous spectrum of wave-vectors, q, of magnitude $2\pi/\lambda$, where λ is the wavelength of the waves that make up the thermal undulations. In order for the surface of each LDH sheet to be described, it is partitioned into a square mesh. The z displacements of the Al^{3+} ions are used to describe the LDH surface by finding the average z coordinate of all Al^{3+} ions in each square grid. The grid segments have an area $a_0 = 36$ Å^2, as this samples twice the frequency of Al^{3+} ions within the sheets; in addition, they are assigned a height function, $h(x, y, n)$. The height function, also known as the Monge representation, can be defined as $h(x, y, n) = z(x, y,$

(46) Helfrich, W. *Z. Naturforsch., C* **1973**, *28*, 693−703.
(47) Lipowsky, R. *Nature* **1991**, *349*, 475−481.
(48) Farago, O. *J. Chem. Phys.* **2003**, *119*, 596−605.

$n) - z_{0,n}$, where $z_{0,n}$ is the mean z displacement of the nth LDH sheet and $z(x, y, n)$ is the average z displacement at the center of each grid segment.[20]

A two-dimensional discrete Fourier transform is carried out on the height function $h(x, y, n)$, which yields the amplitudes, $h(q)$, of all oscillations that make up the thermal undulations as a function of the wave-vector. The Landau−Helfrich free energy can be transformed into Fourier space in order to find the bending modulus, k_c:[20]

$$a_0(|h(\mathbf{q})|^2) = \frac{k_B T}{(\gamma|\mathbf{q}|^2 + k_c|\mathbf{q}|^4)} \tag{9}$$

where the spectral intensity ($|h(\mathbf{q})|^2$) is the mean square of the amplitude of the undulatory modes, k_B is Boltzmann's constant, and T is the temperature of the system.

2.8. Stress−Strain Deformations. An alternative method to study the flexibility of clay sheets using molecular dynamics is to calculate stress−strain curves. This technique was used in the case of montmorillonite to estimate values for the Young's moduli.[20] Hooke's law relates the stress (σ) and strain (ϵ),

$$\epsilon = \mathbf{S}\cdot\sigma \tag{10}$$

where $\mathbf{S}$ is the 6×6 compliance matrix comprising three Poisson's ratios, ν_{yz}, ν_{zx}, and ν_{xy}; three Young's moduli, E_x, E_y, and E_z; and three shear moduli, G_{yz}, G_{zx}, and G_{xy}. We assume that the LDH material has orthotropic symmetry; therefore, it has at least two orthogonal planes of symmetry within which materials properties are independent of direction. This assumption was also made in the case of montmorillonite.[20] It follows that the compliance matrix can be reduced to just nine different components. A set of equations can then be derived to find the directional components of the Young's modulus,

$$\epsilon_{xx} = \frac{\sigma_{xx}}{E_x} - \frac{\nu_{yx}\sigma_{yy}}{E_y} - \frac{\nu_{zx}\sigma_{zz}}{E_z} \tag{11}$$

$$\epsilon_{yy} = \frac{-\sigma_{xx}\nu_{xy}}{E_x} + \frac{\sigma_{yy}}{E_y} - \frac{\nu_{zy}\sigma_{zz}}{E_z} \tag{12}$$

$$\epsilon_{zz} = \frac{-\sigma_{xx}\nu_{xz}}{E_x} - \frac{\sigma_{yy}\nu_{yz}}{E_y} + \frac{\sigma_{zz}}{E_z} \tag{13}$$

$$\epsilon_{yz} = \frac{\sigma_{yz}}{2G_{yz}} \tag{14}$$

$$\epsilon_{zx} = \frac{\sigma_{zx}}{2G_{zx}} \tag{15}$$

$$\epsilon_{xy} = \frac{\sigma_{xy}}{2G_{xy}} \tag{16}$$

where ϵ_{ij} and σ_{ij} are the strain and stress, respectively. If the stress is kept low in two directions, the equations can be simplified in order to plot simple stress vs strain graphs in one dimension, which in turn can be used to determine Young's moduli for the corresponding directions. The elastic moduli were computed for systems **I**, **II**, and **III** by using the final structure at the end of 1.50 ns of molecular dynamics (MD) simulation. The models were expanded and contracted in each dimension. The appropriate cell length was incrementally increased or decreased for each iteration of the simulation, while the other directions were kept at a constant pressure of 1 atm. Atomic positions were rescaled to accommodate the new geometry. The models were deformed at a strain rate of 0.05 ns^{-1}. The simulation box can be deformed at this rate because it is less than the speed of sound in the material, so the relatively high strain rate should not affect any results calculated.

The stress in a solid is defined as the change in internal energy with respect to the strain per unit volume. The stress tensor applied to a linear elastic material is defined as

$$\sigma_{ij} = \frac{1}{V}\left(\frac{\partial E}{\partial \epsilon_{ij}}\right)_S \tag{17}$$

where $(\partial E/\partial \epsilon_{ij})_S$ is the change in energy E with strain ϵ_{ij} at constant entropy S. The stress on the system as a whole is derived from the individual atomic stresses and, therefore, atomic energies. Substituting the individual energy expressions for each atom into eq 17 then leads to the equation[49]

$$\sigma_{kl} = \frac{1}{V}\sum_{i=1}^{N}\left(\frac{m_i}{2}\mathbf{v}_i\mathbf{v}_i + \frac{1}{2}\sum_{j=1}^{N}\mathbf{F}_i\mathbf{r}_{ij}\right)_{kl} \tag{18}$$

where V is the volume, A is the area, m_i is the mass of the ith atom, $\mathbf{v}_i$ is its velocity, $\mathbf{r}_i$ is the position, $\mathbf{F}_i$ is the force on it, and $\mathbf{r}_{ij} = (\mathbf{r}_i - \mathbf{r}_j)$. The sums range over all atoms in the system, and the outer products of the vectors are intended in each term on the right-hand side of eq 18.

Because our system is an intercalated layered structure, it consists of two components: the LDH sheets and the interlayer region. Therefore, using eq 18, we can also calculate the stress applied to the atoms in the clay sheets and, hence, the corresponding elastic moduli. Equation 18 is rewritten as

$$\sigma_{kl} = \frac{1}{h_{clay}A}\sum_{i=1}^{N}\left(\frac{m_i}{2}\mathbf{v}_i\mathbf{v}_i + \frac{1}{2}\sum_{j=1}^{N}\mathbf{F}_i\mathbf{r}_{ij}\right)_{kl} \tag{19}$$

where h_{clay} and A are the thickness and the area of the LDH sheets, respectively. In order to carry out this calculation, we require knowledge of the clay sheet thickness h_{clay}, which we determine from the average distance between the planes defined by the atomic coordinates of the hydrogen atoms on opposite faces of a single sheet. However, this may not be an accurate representation of the clay sheet thickness because it neglects the size of the surface hydrogen atoms. As discussed by Suter[20] et al. and Manevitch and Rutledge[50] for montmorillonite, including the van der Waals radii of the surface atoms can significantly change the calculated Young's moduli. In this study, we present elastic constants for a single LDH sheet calculated with and without the van der Waals radii of surface hydrogen atoms.

(49) Frankland, S. J. V.; Harik, V. M.; Odegard, G. M.; Brenner, D. W.; Gates, T. S. *Comput. Sci. Technol.* **2003**, *63*, 1655−1661.
(50) Manevitch, O. L.; Rutledge, G. C. *J. Phys. Chem. B* **2004**, *108*, 1428−1435.

In addition to Young's moduli, uniaxial deformation yields Poisson's ratios for the material using the resultant strain in the directions transverse to the deformation. If the direction of the deformation occurs along dimension *l*, then the resultant strain occurs in transverse direction *k*. Therefore, the Poisson's ratio, ν_{kl}, is defined as

$$\nu_{kl} = -\left(\frac{\text{lateral strain}}{\text{tensile strain}}\right) = -\frac{\epsilon_k}{\epsilon_l} \tag{20}$$

where ϵ_l is the strain in the direction of uniaxially applied deformation and ϵ_k is the resulting strain in the transverse direction. Using the Poisson's ratios and the Young's moduli, a second, independent value for the in-plane bending modulus can be calculated from the following equation:[20,50]

$$k_i = \frac{E_i h_{\text{clay}}^{\ 3}}{12(1 - \nu_{yx}\nu_{xy})} \tag{21}$$

The index *i* represents either of the in-plane directions *x* and *y*. This method provides validation of the bending modulus obtained from spectral analysis using eq 9. Equation 21 can also be used to determine the correct clay thickness needed to calculate the Young's moduli for the LDH sheets in eq 9. A value for h_{clay} that most closely reproduces the bending modulus calculated from eq 10 will be expected to be the most appropriate with which to compute the Young's moduli of the LDH sheets.

3. Results

3.1. Anionic Hydroxide Sheets. An interesting structural feature considered in the simulations is the alignment of the brucite-like layers with respect to one other. This is relevant to the topic of polytypism in LDH materials.[33] Our model was built from a crystallographic cell consisting of a three-layer rhombohedral structure that had cations in adjacent layers offset by lattice parameters of 2*a*/3, *b*/3 relative to one another;[30] it is interesting to observe whether the structure remains in this alignment during the simulation. Figure 6 shows the distribution of cations in the plane parallel to the clay surface. It is evident from these plots that cations are generally unaligned in adjacent layers, suggesting that the cations are stacked to give the least repulsion between adjacent layers. This type of arrangement is seen for $3R_1$ and $3R_2$ LDH polytypes where the unit cell contains three layers and rhombehedral symmetry, as well as $3H_2$ polytypes that have three layers and hexagonal symmetry.[33] As our models were built using a crystallographic cell with rhombohedral symmetry, the cation stacking suggests that the models have arranged themselves into either a $3R_1$ or $3R_2$ polytype.

Another phenomenon witnessed in our simulations is the presence of "protruding'' Mg^{2+} ions. These atoms account for up to 2% of all magnesium ions in the simulation. Although some Mg^{2+} ions return to their original octahedral positions, most cations stay out of position on the time scale of these simulations by no more than 3 Å. Other authors have also reported similar behavior when using the ClayFF

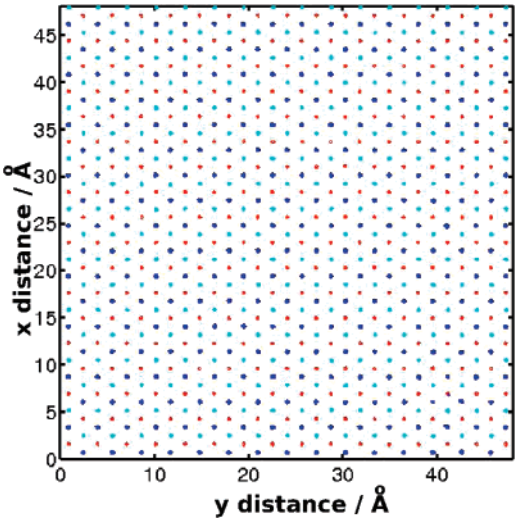

Figure 6. Contour plots in the *xy* plane, parallel to the LDH sheets of system **I** for cationic density, time averaged over the production phase of the simulation. The cations show very little movement over the last 1 ns of simulation. Cyan represents the average distribution of cations in the layer with the lowest *z*-displacement, red cations are in the middle layer, and blue cations are in the top-most layer. The plot shows that the cations in the three LDH layers are stacked in a staggered configuration, giving the least electrostatic repulsion between adjacent layers, which indicates the system has adopted a $3R_1$ or $3R_2$ polytype structure.[33]

forcefield.[24,51] The protruding ions are distributed randomly rather than being clustered within a particular domain. We are unaware of any direct experimental evidence for this phenomenon in Mg_2Al-LDH. However, in other LDHs, such as Ca,Al-hydrocalumite, the M^{2+} cations have been found in experiment and simulation to form 7-coordinate environments.[52] Earlier work using the Dreiding forcefield by Newman et al.[15] also suggested that atom displacement can occur. Indeed, the Ca,Al-LDHs show that the majority of Ca^{2+} ions can be displaced to 7-coordinate sites adjacent to the interlayer, where water molecules provide the additional coordination component. One might infer that the closer match in ionic radii between Mg^{2+} (0.072 nm) and Al^{3+} (0.053 nm) relative to Ca^{2+} (0.099 nm) and Al^{3+} would result in better packing with reduced, but not total loss of, Mg^{2+} ion displacement.

3.2. Behavior of Intragallery Molecules. The intragallery water molecules behave like a confined two-dimensional liquid while trapped between the sheets of the LDH. There are also strong hydrogen bonds between the surface of the clay and the oxygen atoms of the water, which constrain the movement of the water molecules further. Self-diffusion coefficients are given in Table 3. Although the basal spacing is essentially independent of system size, the diffusion coefficients increase at larger system sizes. Although increasing the system size of molecular dynamics simulations with periodic boundary conditions can cause self-diffusion coefficients to increase,[53] the increase we find at large system size we tentatively attribute to thermal undulations, which

(51) Lombardo, G. M.; Pappalardo, G. C.; Punzo, F.; Costantino, F.; Costantino, U.; Sisani, M. *Eur. J. Inorg. Chem.* **2005**, *24*, 5026−5034.
(52) Kalinichev, A. G.; Kirkpatrick, R. J.; Cygan, R. T. *Am. Mineral.* **2000**, *85*, 1046−1052.
(53) Yeh, I. N.; Hummer, G. *J. Phys. Chem. B* **2004**, *108*, 15873−15879.

Table 3. Properties of the System Averaged over 1 ns of Simulation and Errors Found from the Standard Deviation; Basal Spacing and Self-Diffusion Coefficients of Water Molecules in the Interlayer Region for All Model Sizes (Unlike the Basal Spacing, the Diffusion Coefficients Increase at Larger System Sizes)

system	basal spacing (Å)	self-diffusion coefficient ($m^2\ s^{-1}$)
I	8.97 ± 0.02	$6.1 \pm 0.1 \times 10^{-11}$
II	8.928 ± 0.006	$6.1 \pm 0.2 \times 10^{-11}$
III	8.943 ± 0.003	$8.0 \pm 0.2 \times 10^{-11}$
IV	8.978 ± 0.001	$9.33 \pm 0.03 \times 10^{-11}$

imparts enhanced motion on the water molecules. To our knowledge, there is no direct experimental data for our system, although experimental studies using quasi-elastic neutron scattering (QENS) and nuclear magnetic resonance (NMR) methods have been carried out on hydrotalcite-like materials intercalated with other ions.[54,55] Mg_2Al-LDH intercalated with nitrate ions yielded water diffusion coefficients of 3×10^{-11} m ^{2} s^{-1},[55] whereas Mg_2Al-LDH intercalated with carbonate ions produced a value of 1.44×10^{-11} m ^{2} s^{-1}.[54]

The visualization in Figure 5a of the interlayer region, and the atomic density profiles in Figure 7, show that the interlayer region has structure. The atomic density profile represents the distribution of atoms along the *z* axis, which is perpendicular to the LDH surface. Molecules form two layers within the interlayer. The region closest to the clay layer generally contains oxygen atoms from water molecules and chloride ions as shown in the atomic density profiles. The atomic density profiles also show that there is an equal probability of the surface being covered by chloride ions or oxygen atoms. The peaks in the atomic density profile also broaden with system size, caused by the emergence of thermal undulations.

In Figure 8, we present calculated powder X-ray diffraction patterns for the two smallest systems in our study using the diffraction-crystal module of Cerius.[1] We have included the experimental XRD obtained by Vera and Pinnavaia[36] for comparison. It must be borne in mind that our simulations provide an idealized model for LDH compounds. Our study is primarily concerned with size effects; therefore, at large sizes, we do not include nonhomogeneous charge distribution, interstratification, or turbostratification in our simulations, all of which may cause the presence of many hydration states of interlayer cations within the same sample. These effects will lead to broad peaks in experimental diffractograms. Our simulations show a single, well-defined peak, which is close to the limits of the peak found experimentally. Therefore, we can conclude that our simulations correctly represent LDH sheets, albeit somewhat idealized ones.

3.3. Sheet Undulation Spectral Intensity Analysis. The LDH system in this study is anisotropic. Therefore, to understand the behavior of the material, the spectral intensity was decomposed in the *x* and *y* dimensions and graphs of $a_0\langle|h(q_x)|^2\rangle$ vs q_x and $a_0\langle|h(q_y)|^2\rangle$ vs q_y were plotted. The spectral intensity was first calculated and averaged over each snapshot of the simulation and then averaged over each layer. The results are shown in parts a and b of Figure 9.

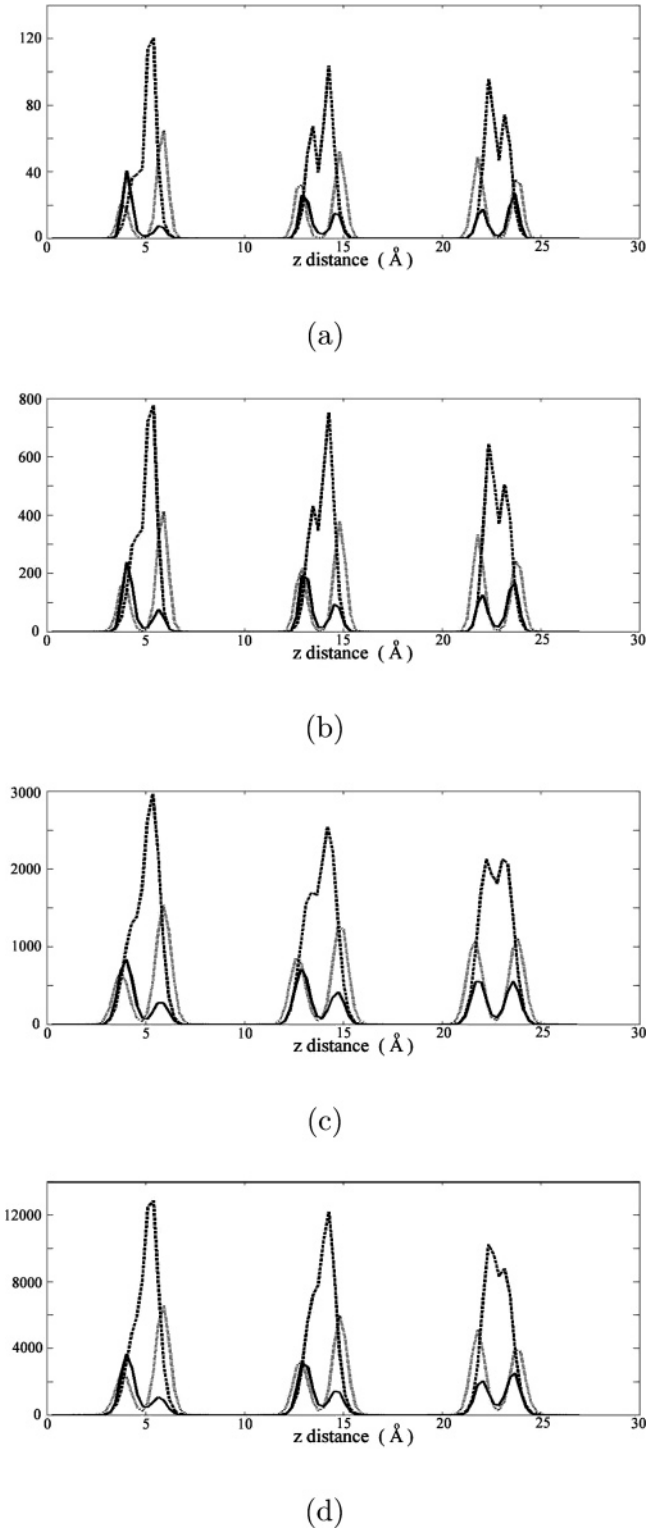

Figure 7. Atomic density profiles for (a) system **I**, (b) system **II**, (c) system **III**, and (d) system **IV**, in the *xz* plane. The bold line represents chloride ions, the light gray line represents oxygen atoms of water, and the dotted line represents hydrogen atoms of water. The graphs show that the interlayer has a well-defined structure, with oxygen and chloride ions closest to the clay sheets and hydrogen atoms close to the midplane. The peaks of the atomic density profiles become more indistinct with system size because of the thermal undulations.

(54) Kagunya, W. W. *J. Phys. Chem.* **1996**, *100*, 327−330.
(55) Marcelin, G.; Stockhausen, N. J.; Post, J. F. M.; Schutz, A. *J. Phys. Chem.* **1989**, *93*, 4646−4650.

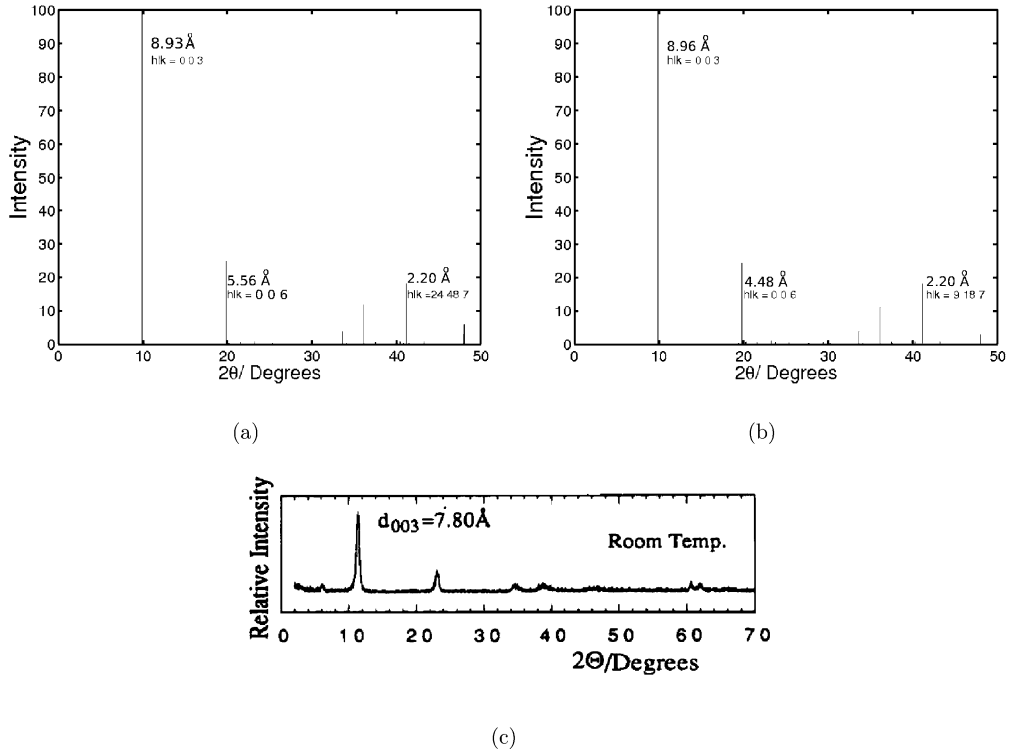

Figure 8. Simulated powder X-ray diffraction spectra for (a) system **I** and (b) system **II** compared with (c) experimental values collected by Vera and Pinnavaia.[36] Discrepancies exist between the simulated and experimental basal spacing, which we attribute to the idealized nature of our simulations. Our simulation models do not include effects such as nonhomogeneous charge distribution, interstratification, or turbostratification, all of which may cause the presence of many hydration states of interlayer cations within the same sample. These effects will lead to a broad peak in the experimental diffractogram. Our simulations show a single, well-defined peak, which is close to the limits of the peak found experimentally.

Table 4. In-plane Elastic Constants in GPa Calculated from the Stress−Strain Behavior of (i) the Whole System Containing the Clay Framework Plus Interlayer and (ii) the Clay Sheet Elements (a) Not Including and (b) Including the Van Der Waals Radius of Hydrogen Atoms; Error Bars Are Determined from the Least-Squares Fit

			(ii) LDH sheet			
	(i) LDH sheet and interlayer		(a) $h_{clay} = 4.05$ Å		(b) $h_{clay} = 6.45$ Å	
system	E_x (GPa)	E_y (GPa)	E_x (GPa)	E_y (GPa)	E_x (GPa)	E_y (GPa)
I	64.3 ± 0.2	60.2 ± 0.4	139.2 ± 0.5	140.5 ± 0.9	90.6 ± 0.4	88.2 ± 0.9
II	63.3 ± 0.1	64.0 ± 0.2	138.3 ± 0.4	137.8 ± 0.6	86.8 ± 0.3	86.5 ± 0.4
III	63.89 ± 0.07	64.6 ± 0.1	137.0 ± 0.2	139.2 ± 0.4	86.0 ± 0.2	87.4 ± 0.3

The graphs show that the q^{-4} dependence predicted from eq 9 is seen at higher wave-vector values rather than lower ones. Parts a and b of Figure 9 yield a value for the bending modulus of $\sim 1 \times 10^{-19}$ J, although the large degree of noise at higher wave-vectors makes the calculated value of the bending modulus rather approximate. This result shows that hydrotalcite-like materials are about 2 orders of magnitude more flexible than montmorillonite clays, while being an order of magnitude less flexible than lipid bilayers.[20] Compared to smectite clays like montmorillonite, the atoms within the LDH sheet are less tightly bound together than within montmorillonite, making it much easier for the layers to bend.

Increasing the system size introduces a q^{-2} behavior at shorter q and higher wavelengths. At large enough length scales, adjacent layers will start to interact with one another, resulting in the damping of thermal undulations.[20,56] When the interaction between the layers is taken into account, the free energy can be equated to[20]

$$F = \sum_{n=0}^{N-1} \int_A \mathrm{d}x\, \mathrm{d}y \left[\frac{k_c}{2} \left(\frac{\partial^2 h_n}{\partial x^2} + \frac{\partial^2 h_n}{\partial y^2} \right)^2 + \frac{B}{2} (h_n - h_{n+1})^2 \right] \quad (22)$$

where N represents the number of layers in the system and B is the compressibility modulus perpendicular to the surface of a single sheet. The second term in the integrand and on the right-hand side of eq 22 represents the approximate free energy of compression. The in-plane correlation length ξ is used to characterize the point at which the thermal undulations are large enough to cause layer−layer interactions;[56] ξ is defined as $(k_c/B)^{1/4}$. The generalization implied by eq 22 means that eqs 9 now becomes

$$a_0 \langle |h(q)|^2 \rangle = \frac{k_B T}{k_c q^4} \left[1 + \frac{4}{(\xi q)^4} \right]^{-1/2} \quad (23)$$

The crossover point when the spectral intensity changes from q^{-4} to q^{-2} is defined by the wave-vector $q_c = 2\pi/\xi$.

(56) Loison, C.; Mareschal, M.; Kremer, K.; Schmid, F. *J. Chem. Phys.* **2003**, *119*, 13138−13148.

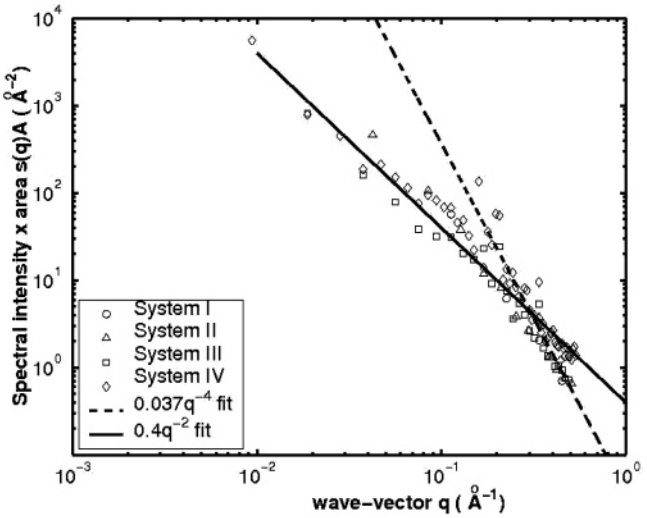

(a)

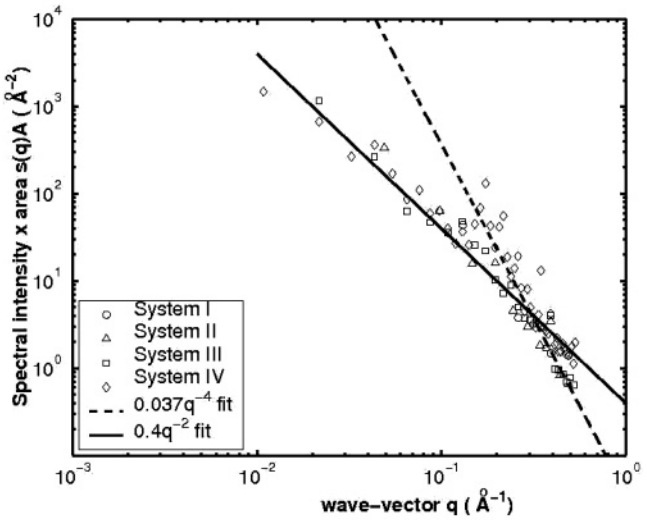

(b)

Figure 9. Spectral intensity per undulatory mode versus wave-vector (q) in (a) x and (b) y directions for systems **(I**, **II**, **III**, **and IV)**. The dashed line represents the q^{-4} undulatory modes for $q > 0.2$. The resulting bending modulus for this fit is $k_c \approx 1 \times 10^{-19}$ J. At lower wave-vectors, the intensity behaves as q^{-2} as the thermal undulations are damped by interactions between adjacent clay layers.

We find a value for $q_c \approx (0.4/0.037)^{-1/2}$, which means $\xi \approx$ 20.7 Å. This value is relatively small compared to the value calculated for montmorillonite, which was >1000 Å.[20] This can be attributed to the smaller bending rigidity of LDH compared to montmorillonite, which has a bending modulus of 1.6×10^{-17} J. The narrow distance between the LDH sheets of ~4 Å also contributes to an increase in compressibility modulus, with both factors leading to a much lower in-plane correlation length.

3.4. Stress−Strain Deformations. The stress−strain graphs derived in this section (see Figure 10) aim to provide values for the in-plane Young's moduli in the x and y dimensions. We also determine separate Young's moduli for the LDH sheets and the whole system. Using eq 18, we calculated Young's moduli for a single LDH sheet. A value of 4.05 Å was used as the thickness of each LDH sheet, determined from the atomic density profiles. Table 5 shows that the system as a whole is much more flexible than the LDH sheets. Determining the precise thickness of the LDH sheets is important as it affects values for the Young's modulus.[20] If we take into account the van der Waals radius of the hydrogen atoms at 1.2 Å,[57] then the layer thickness is 6.45 Å. Using the two values for layer thickness, Young's moduli for the LDH sheets are estimated to be 138.7 ± 0.5 GPa for a layer thickness of 4.05 Å and 87.6 ± 0.5 GPa for a layer thickness of 6.45 Å. Using an atom-centered layer thickness means that the load applied to the sheets is carried at the center of each atom.[50]

Comparison with spectral intensity results helps determine which h_{clay} value to use for the calculation of the Young's modulus. The spectral intensity yields an approximate value of the bending modulus to be $\sim 1 \times 10^{-19}$ J. The Poisson's ratio as well as the Young's modulus can be used to extract the bending modulus, as show by eq 21. Table 6 shows that including the hydrogen van der Waals radius within the thickness of the LDH sheets increases the bending modulus by an order of magnitude. Using the atom centers for the bending modulus calculation shows better agreement with the spectral intensity results. Experimentally, the thickness of Mg_2Al-LDH sheets has been found by measuring the orthogonal distance to the plane between cations and oxygen atoms on a single sheet. Bellotto et al. report this value to be 1.9587 Å.[30] In brucite, the same distance is 2.11 Å and the total layer thickness of is 4.77 Å,[36] so the extra distance between oxygen and hydrogen atoms is 0.275 Å. Assuming that O−H distances are the same for brucite as for LDH, the total experimental layer thickness is 4.47 Å. The simulated atom-centered thickness is then in much better agreement with the experiment, making it more likely to produce an accurate value for the elastic constants. Therefore, the in-plane bending modulus is most likely to be $8.28 \pm 0.07 \times 10^{-19}$ J.

In general, decomposing the Young's modulus in the x and y dimensions makes little difference to the Young's modulus. The LDH sheets plus interlayer region have a Young's modulus in the x dimension of 63.83 ± 0.1 GPa and 62.9 ± 0.2 GPa in the y dimension. The isolated LDH sheets show an increase in flexibility with model size in the x dimension, but not in the y dimension. Increased flexibility may be indicative of the development of thermal undulations, which cause the sheets to become more easily expandable or compressible. Although the most linear portion of the stress−strain curve has been used to calculate the Young's modulus, this section of the graph can be difficult to estimate. The errors reported in Table 4 do not take this into account, so the increase in Young's moduli in the x dimension may be due to systematic errors rather than finite-size effects. Similarly the Poisson's ratios reported in Table 6 show a small decrease in the y dimension with system size, whereas a slight increase is seen in the x dimension. We attribute the slight change in Poisson's ratio with system size to systematic errors in determining the slope of $-\epsilon_k/\epsilon_l$. The average Poisson ratio for all systems is 0.295 ± 0.003.

(57) Pauling, L. *The Nature of the Chemical Bond and the Structure of Molecules and Crystals; An Introduction to Modern Structural Chemistry*, third ed.; Cornell University Press: Ithaca, NY, 1960.

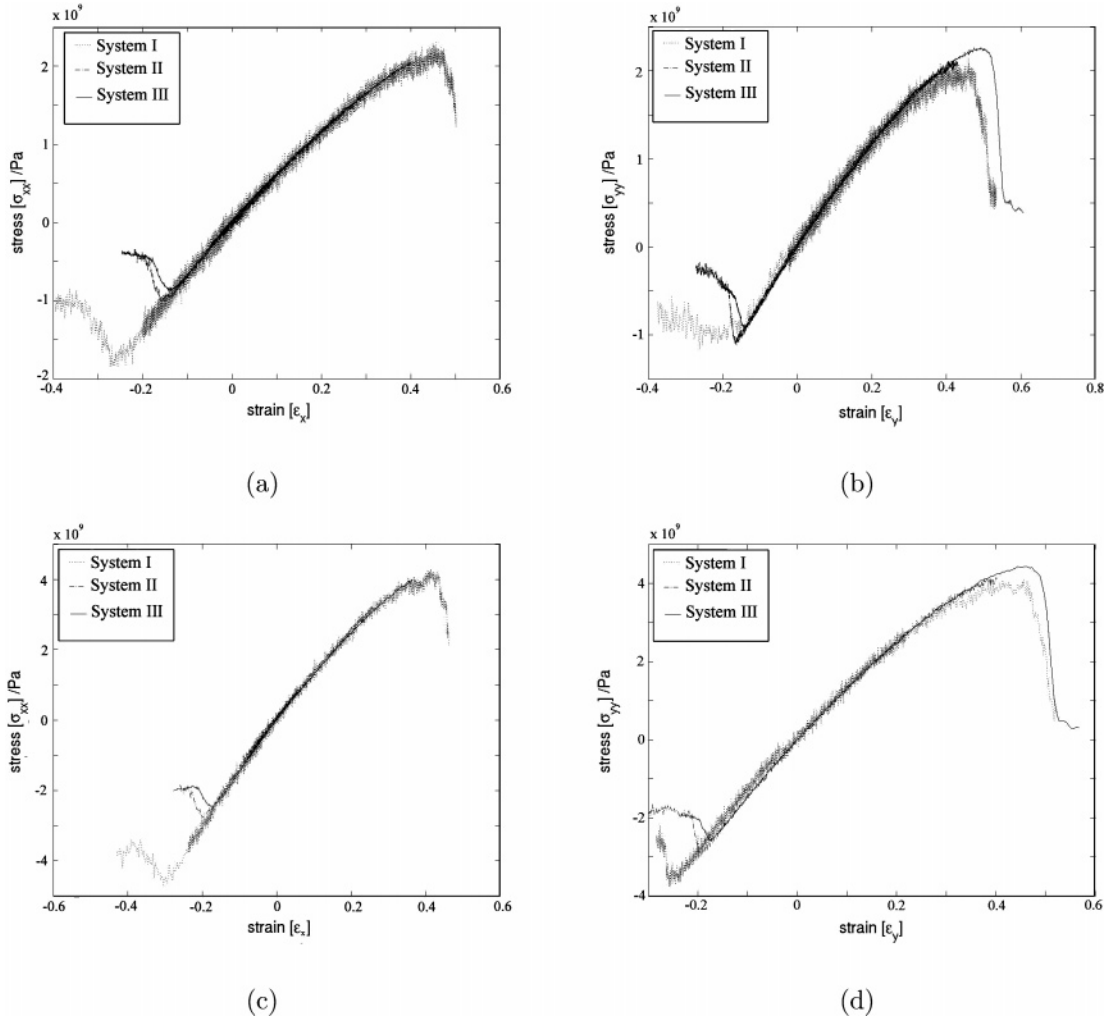

Figure 10. Stress−strain graphs for systems **I**, **II**, and **III**. (a) Represents the stress as a function of strain for the clay sheets and interlayer region in the *x* direction, and (b) represents the stress vs strain in the *y* direction; (c) represents the stress vs strain for the clay sheets alone in the *x* direction, and (d) represents that in the *y* direction. The gradient of the stress−strain curves produces Young's moduli values for each respective direction of the LDH material.

Table 5. Poisson's Ratio of Each System, Calculated from the Resultant Strain in the Transverse Direction to Direction of the Uniaxial Deformation[a]

	Poisson's ratio	
system	ν_{yx}	ν_{xy}
I	0.285 ± 0.002	0.313 ± 0.006
II	0.293 ± 0.004	0.294 ± 0.005
III	0.3028 ± 0.0009	0.2828 ± 0.0006

[a] The average Poisson's ratio for all systems is 0.295 ± 0.003. The Poisson's ratios are similar for all systems. Error bars are determined from the least-squares fit.

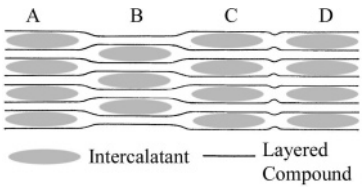

Figure 11. Diagram that shows a Daumus−Hérold structure for a stage-2 layered compound,[66] where bulky intercalants reside in all layers but form domains, shown in the diagram as A, B, C, and D. LDHs have been shown to adopt second-order staging, which occurs when only every other layer is filled with intercalant.

The small size of LDH platelets makes it difficult (if not impossible) to obtain materials properties like the Young's moduli using conventional experimental techniques: currently, no experimental data are available for comparison. However, we can make a comparison with brucite for which the elastic stiffness matrix has been obtained by Brillouin scattering,[58] which produced values for C_{11} and C_{12} of 156.7 and 44.4 GPa, respectively. The Young's modulus in the *x* dimension can be calculated from the equation $E_x = (C_{11} + 2C_{12})(C_{11} - C_{12})/(C_{11} + C_{12})$, from which E_x for brucite is found to be 137 GPa. Unlike LDHs, the interlayer of brucite does not contain water and counterions that would be expected to reduce the C_{11} parameter, but this value is nevertheless in good agreement with the Young's modulus calculated for LDH sheets. More rigid materials, such as smectite clays, have Young's moduli around two times larger than those of LDHs.[20] By the same token, LDHs are less flexible than graphite, which has a Young's modulus of ∼12 GPa. We note in passing that Sato et al.[59] performed a small length- and time-scale MD study of fracture within a single cationic clay layer under applied stress, achieving reasonable agreement with atomic force microscopy observations of the curvature of the sheet prior to fracture.

(58) Xia, X.; Weidner, D. J.; Zhao, H. *Am. Mineral.* **1998**, *83*, 68−74.
(59) Sato, H.; Yamagishi, A.; Kawamura, K. *J. Phys. Chem. B* **2001**, *105*, 7990−7997.

Table 6. Bending Moduli of Each System Calculated from the Poisson's Ratios and Young's Moduli; the Smaller Value of h_{clay} in (a) Corresponds to the Thickness of the LDH Sheets, Computed from Opposing Hydrogen Atom Centers on the LDH Surface, while the Larger Value in (b) Includes the Hydrogen Van Der Waals Radius[a]

	bending modulus (J)			
	(a) $h_{clay} = 4.05$ Å		(b) $h_{clay} = 6.45$ Å	
system	k_x	k_y	k_x	k_y
I	$8.5 \pm 0.2 \times 10^{-19}$	$7.8 \pm 0.2 \times 10^{-19}$	$2.22 \pm 0.05 \times 10^{-18}$	$1.99 \pm 0.04 \times 10^{-18}$
II	$8.4 \pm 0.2 \times 10^{-19}$	$8.3 \pm 0.2 \times 10^{-19}$	$2.12 \pm 0.05 \times 10^{-18}$	$2.11 \pm 0.05 \times 10^{-18}$
III	$8.3 \pm 0.03 \times 10^{-19}$	$8.4 \pm 0.04 \times 10^{-19}$	$2.189 \pm 0.09 \times 10^{-18}$	$2.14 \pm 0.01 \times 10^{-18}$

[a] Results from (a) agree more closely with the spectral intensity analysis than the results from (b), suggesting that the load applied to the sheets is carried by the atom centers.

4. Discussion and Conclusions

High-performance grid-based computing has given us the opportunity to model Mg_2Al-LDH platelets 58×67 nm in size, approaching the lateral dimensions of real LDH platelets, which are around 100−200 nm in length.[60] We found that the interlayer spacing is a property that is not affected by size. However, the computed diffusion coefficients for water increase at larger system sizes, suggesting that water molecules then have a greater mobility. Another structural feature that we computed was the stacking arrangement of cations within adjacent LDH sheets. This analysis showed that, in all models, the cations were stacked such that they avoid alignment with each other. The stacking arrangement adopted by the system is an important structural feature in the discussion of polytypism. Our system was originally based on a crystallographic unit cell consisting of three layers in a rhombohedral space group, although the exact stacking arrangement was not known. As the cations arrange themselves in a staggered configuration, this indicates that the models are adopting a $3R_1$ or $3R_2$ polytype structure.[33]

While these properties are size independent, emergent behavior was witnessed that would otherwise be suppressed in smaller simulations. Our study has shown that thermal undulations become more pronounced for larger system sizes although, at a wavelength of ~20.7 Å, these undulations are damped because of interaction with neighboring layers. Analysis of thermal undulations yields an estimate for the bending modulus of $k_c \approx 1 \times 10^{-19}$ J.

Deforming the models in the *x* and *y* dimensions produces stress−strain behavior that can be used to determine the Young's moduli of the material in each respective dimension. The in-plane Young's modulus for the clay-plus-interlayer region was found to be 63 and 139 GPa for the LDH sheets alone. The Young's moduli and Poisson's ratio together determine a more accurate value for the in-plane bending modulus of $8.28 \pm 0.07 \times 10^{-19}$ J. These results show that the Mg_2Al-LDH in our study is more flexible than montmorillonite, whose in-plane Young's modulus was estimated to be 170−190 GPa for the combined clay-plus-interlayer structure and 230 GPa for the clay sheets alone.[20] As with smectite clays, the elastic moduli determined in this study may be applied in the area of clay−polymer nanocomposites, where interest is growing in the use of LDHs as nanofillers,[61] for which an accurate knowledge of the elastic moduli of each component is required.

The techniques described in this paper may be used in the future to calculate materials properties for LDH/polymer systems, many of which have not yet been studied experimentally. LDHs have attracted considerable interest as possible hosts for biopolymers such as nucleic acids and long-chain surfactants. The flexibility of LDHs, as demonstrated in this paper, makes it possible to intercalate bulky anions such as biopolymers. Although LDHs are not as flexible as graphite, it is clear from the results in this paper that they are considerably more flexible than smectite clays like montmorillonite. A phenomenon affected by flexiblity is the process of staging, and as a consequence, it is often evident in graphite intercalation compounds but not in smectite clays.[62,63] Staging is the process by which compounds intercalate within layered materials such as graphite.[64] Staging is believed to occur in graphite via a domain model proposed by Daumus and Hérold, as shown in Figure 11.[65−67] The intercalant molecules are thought to diffuse toward the center of the crystal. Although not evident in cationic clays, various LDHs, including Mg_2Al-LDH intercalated with organic molecules, have been shown to form second-stage intermediates.[67−69] Second-order staging occurs when every second layer is filled with intercalant, but no higher-order staging phenomena have been reported. So far, experimental studies have been unable to determine the exact mechanism by which staging occurs in LDHs. Future simulation studies may enable us to investigate this phenomenon and explore whether a Daumus−Hérold structure can be seen for LDHs intercalated with bulky biopolymers.[60]

Acknowledgment. This work was in part supported by the U.K. Engineering and Physical Sciences Research Council (EPSRC) (GR/T27488/01), which also provided access to HPCx (www.hpcx.ac.uk). We are also indebted to the National Science Foundation for TeraGrid allocations under NRAC Grant MCA04N014, utilizing resources on the U.S. TeraGrid

(60) Kwak, S.-Y.; Kriven, W. M.; Wallig, M. A.; Choy, J.-H. *Biomaterials* **2004**, *25*, 5995−6001.
(61) Leroux, F.; Besse, J.-P. *Chem. Mater.* **2001**, *13*, 3507−3515.
(62) Solin, S. A. *Ann. Rev. Mater. Sci.* **1997**, *27*, 89−115.
(63) Schon, J. C.; Adler, D.; Dresselhaus, G. *J. Phys. C: Solid State Phys.* **1988**, *21*, 5595−5614.
(64) Misenheimer, M. E.; Zabel, H. *Phys. Rev. Lett.* **1985**, *54*, 2521−2524.
(65) Safran, S. A. *Phys Rev. Lett.* **1980**, *44*, 937−940.
(66) Kirczenow, G. *Phys. Rev. Lett.* **1982**, *49*, 1853−1856.
(67) Pisson, J.; Taviot-Gueho, C.; Israeli, Y.; Leroux, F.; Munsch, P.; Itie, J.-P.; Briois, V.; Morel-Desrosiers, N.; Besse, J.-P. *J. Chem. Phys B* **2003**, *107*, 9243−9248.
(68) O'Hare, D. O.; Evans, J. S.; Fogg, A.; O'Brien, S. *Polyhedron* **2000**, *19*, 297−305.
(69) Iyi, N.; Kurashima, K.; Fujita, T. *Chem. Mater.* **2002**, *14*, 583−589.

(www.teragrid.org), the U.K.'s National Grid Service (www.ngs.ac.uk), and the DEISA Consortium (cofunded by the EU, FP6 project 508830) within the DEISA Extreme Computing Initiative (www.deisa.org). We are grateful to Andrey Kalinichev at the University of Illinois at Urbana−Champaign for supplying energy-minimized structures of the layered double hydroxides used in this study. We thank David Vowles at the University of Cambridge for providing SEM images of organo-LDHs. M.-A.T. was funded by an EPSRC Ph.D. studentship associated with the RealityGrid Project (GR/67699/02 and EP/C536452/01).

Supporting Information Available: MPEG animations of height functions of systems (**I**−**IV**) and MD trajectories for 0−2 ns of systems (**I**−**IV**) with *z* expansion factor of 3 are included in the Supporting Information. This material is available free of charge via the Internet at http://pubs.acs.org.

CM070923U